Discover Materials

RESEARCH Open Access

# Optimization of post-processing parameters for enhanced characterization in metal extrusion 3D printing of copper-polymer composites

Syed Fouzan Iftekar[1,2], Abdul Aabid[3*], Nor Aiman Sukindar[2], Adibah Amir[2] and Muneer Baig[3]

*Correspondence:
Abdul Aabid
aaabid@psu.edu.sa
[1]Department of Mechanical Engineering, Universiti Teknologi PETRONAS, Seri Iskandar, 32610 Perak, Malaysia
[2]Manufacturing and Materials Department, Kulliyyah of Engineering, International Islamic University Malaysia, Jln Gombak, 53100 Kuala Lumpur, Malaysia
[3]Department of Engineering Management, College of Engineering, Prince Sultan University, PO BOX 66833, 11586 Riyadh, Saudi Arabia

**Abstract**
The high costs associated with metal additive manufacturing methods including expensive feedstock, energy-intensive lasers, and controlled environments have limited their widespread adoption in industries like aerospace and automotive, despite powder bed fusion success in producing intricate and high-precision components. As a cost-effective alternative, material extrusion 3D printing enables the fabrication of metal-polymer composites using simpler equipment. However, challenges remain in optimizing post-processing parameters to enhance mechanical performance and microstructural integrity. This study focuses on improving the post-processing of copper-filled PLA parts fabricated with an Artillery Sidewinder X1 material extrusion printer. A Taguchi design of experiments approach using an $L_8$ orthogonal array was employed to investigate the effects of debinding time, sintering time, and layer thickness. Results showed that shorter debinding compromised structural integrity in 25% of samples, while optimized settings achieved a 30.59% shrinkage and a 12.5% hardness increase. These findings highlight the significance of proper thermal post-processing in controlling dimensional changes and improving part quality.

**Keywords** 3D Printing, Additive manufacturing, Metal, Polymer, Material extrusion, Debinding, Sintering

## 1 Introduction

Additive Manufacturing (AM) is an emerging technology defined by ASTM as the process of joining materials layer by layer to create objects from a computer-aided design (CAD) model. The ASTM classifies AM into seven categories: material extrusion, powder bed fusion, directed energy deposition, material jetting, binder jetting, vat photopolymerization, and sheet lamination [1, 2]. AM is a layer-by-layer fabrication technology that enables the creation of complex geometries directly from CAD models. According to the ISO/ASTM 52900:2021 standard, AM processes are classified into seven

categories: Vat Photopolymerization, Material Jetting, Binder Jetting, Material Extrusion, Powder Bed Fusion, Sheet Lamination, and Directed Energy Deposition [3, 4]. This classification serves as the global standard for distinguishing AM process types based on their fundamental operating principles. Among metal AM techniques, Powder Bed Fusion (PBF) is well-known for producing intricate, high-precision components but is often limited by high material and operational costs. In contrast, Material Extrusion (MEX) provides a more accessible and economical option for fabricating metal-polymer composite parts, making it a suitable candidate for post-processing optimization studies. In this study, we focus specifically on MEX as a cost-effective method for metal-polymer composite fabrication.

Critically explore post-processing and parameter optimization in additive manufacturing. Alzyod et al. [4] and Alzyod and Ficzere [5, 6] utilized Box–Behnken Design to enhance the MEX ironing process, improving surface finish and strength, though print time trade-offs were not fully assessed. Andreacola et al. [7] examined binder jetting of 17–4 PH steel, linking process parameters to mechanical properties but lacking practical validation. Raza et al. [8] proposed hybrid microwave-thermal treatment for FDM parts, achieving notable tensile improvements while omitting cost-efficiency analysis. Each study highlights parameter control as key to AM performance. However, energy use and industrial scalability remain underexplored. Together, these works advance AM post-processing but call for broader benchmarking and lifecycle analysis. Nguyen and Lee [9] proposed a chemical treatment, drying, and aluminum coating hybrid method that achieved a surface roughness of 2.06 μm and improved thermal reflectivity for thermoforming molds. The third study targeted FDM PLA parts, optimizing path speed, ironing spacing, and flow rate, significantly enhancing surface smoothness through ironing post-processing [8].

Previous studies offered numerous recommendations for enhancing and optimizing post-processing parameters for 3D printed metal composites yet research on post-processing of metal-polymer composites remains limited. Material Extrusion (MEX) technologies employ different mechanisms, including screw-based, piston-driven, and pinch-wheel systems. Screw-based systems enable precise control over material flow, ideal for high-viscosity metal-polymer composites, while piston-driven mechanisms ensure consistent pressure for extruding dense metallic pastes. In contrast, pinch-wheel systems, common in polymer extrusion, often struggle with the rigidity of metal-filled filaments. Recent studies, such as those by Drummond et al. [10] on cast iron and Lozhkomoev et al. [11] on sintering parameters, has shown that screw and piston driven MEX systems are particularly effective for producing high-quality metal parts, underscoring their role in metal-polymer fabrication. Similarly, Kolli et al. [12] developed a paste-based micro-extrusion technique for pure copper, attaining 98% post-processing density using a propanol binder—a result underscoring the potential of MEX for dense metallic structures. These advances highlight the growing role of MEX in fabricating complex geometries, though challenges persist in post-processing to ensure mechanical integrity and functional performancePost-processing remains a critical bottleneck for metal-polymer composites.

Khosravani et al. [13] emphasized its impact on dimensional accuracy and structural reliability, noting that parameter optimization is essential to mitigate defects like porosity and cracking. This is evident in studies such as Raza et al. [8], who identified

process-induced brittleness and cracks in MEX-printed 316L stainless steel, and Atatreh et al. [14], who demonstrated how triangular infill patterns in MEX can reduce production costs while maintaining structural efficiency. In the biomedical sector, Shamsudin et al. [15] optimized PLA/SS316L composites for orthopedic implants, achieving enhanced tensile strength through tailored printing parameters. However, Wu et al. [16] revealed that even meticulous process chain adjustments for 316L stainless steel composites could not fully eliminate porosity without targeted post-processing.

Recent industrial advancements in post-processing include techniques like Hot Isostatic Pressing (HIP) to eliminate porosity [10] and bronze infiltration to improve conductivity [17]. Surface treatments such as electroplating and chemical passivation have also been employed to refine corrosion resistance and biocompatibility [15, 16]. However, these methods often require costly specialized equipment, limiting accessibility for small-scale industries. In contrast, foundational steps like debinding and sintering—critical for ensuring uniform density and minimizing downstream defects—remain understudied. For example, Lozhkomoev et al. [11] showed that sintering duration directly influences density in MEX parts, with samples reaching 94.6% relative density after optimized cycles. Yet, inconsistencies in sintering parameters across studies underscore the need for standardized protocols.

Previous studies on metal-polymer mixtures have mainly used stainless steel. Mogan et al. [18] tested steel-reinforced plastic but found that adding more metal reduced strength—a mix with 10% steel had 38 MPa strength, far below pure steel's 500–700 MPa. This shows the difficulty of bonding plastics and metals,a problem worsened by copper's tendency to oxidize and conduct heat during processing. Similarly, Opoz et al. [19] improved the strength of stainless-steel parts to 1242 MPa through heat treatment, but leftover pores and rough surfaces caused brittle fractures. These findings highlight the need for customized processing methods for different materials. Another challenge is inconsistent sintering conditions. Lozhkomoev et al. [11] achieved higher part density (94.6%) with longer sintering times, but varying temperatures and methods across studies make results hard to repeat. Sadaf et al. [20] stressed the need for standardized steps to ensure reliable part quality. For copper, precise control of sintering conditions is critical to avoid oxidation and uneven density due to its high heat conductivity. By studying Cu-PLA composites, this work aims to solve these issues, improving post-processing methods to meet industrial needs. The results could provide a reliable way to create high-density copper parts from 3D-printed composites, offering industries an affordable option for complex, high-performance components. This bridges the gap between innovative design possibilities and practical manufacturing requirements.

## 2 Materials and methods

This study focuses on optimizing post-processing parameters (debinding time and sintering time) along with the printing parameter of layer thickness to evaluate their combined influence on the structural and mechanical performance of copper-PLA parts.

### 2.1 Metal filaments

The metal filament used in this research is a copper-polymer composite composed of 90 wt% pure copper powder and 10 wt% polylactic acid (PLA) binder, forming a 9:1 ratio. The filament has a diameter of 1.75 mm and a density of 4.8–5.0 g/cm$^3$. A particle size

distribution analysis of the copper powder revealed a mean particle size of 32 µm, with a broad distribution ranging from 2 µm to 62 µm (32 ± 30 µm). The copper powder exhibits a spherical morphology, which enhances packing density and contributes to high thermal and electrical conductivity in the final sintered parts.The PLA binder, a biodegradable thermoplastic, ensures uniform dispersion of the copper particles and provides structural integrity during printing. This feedstock is compatible with standard material extrusion (MEX) 3D printers. For this study, printing was performed using an Artillery 3D Sidewinder X1 printer, which features a build volume of 300 × 300 × 400 mm, a heated build plate capable of 130 °C, and a nozzle temperature of up to 240 °C.

Post-processing steps, including debinding and sintering, are critical for converting the 3D-printed green parts into dense metallic components. Sintering temperatures reached 1052 °C (1925°F), enabling atomic diffusion and pore elimination within the copper powder matrix [21]. The copper-PLA composite filament was sourced from Virtual Foundry (USA).

### 2.2 Sample preparation

The experiment comprised eight samples, with four having a layer thickness of 0.3 mm and the remaining four with 0.4 mm. Layer thickness was varied to assess its impact on shrinkage, weight loss, and other parameters. Using Blender software, uniform dimensions of 25 mm length, 25 mm width, and 5 mm height were maintained, as illustrated in Fig. 1A.

The selection of 0.3 mm and 0.4 mm layer thicknesses was based on preliminary tests and recommendations from literature, which suggest that thinner layers offer better surface finish and dimensional accuracy, while thicker layers provide improved thermal stability during post-processing and reduce print time [22].

An infill density of 80% was selected to optimize material usage and part durability, as shown in Fig. 1C. This density was chosen based on empirical evidence and preliminary tests indicating that it provided good balance between structural integrity and material

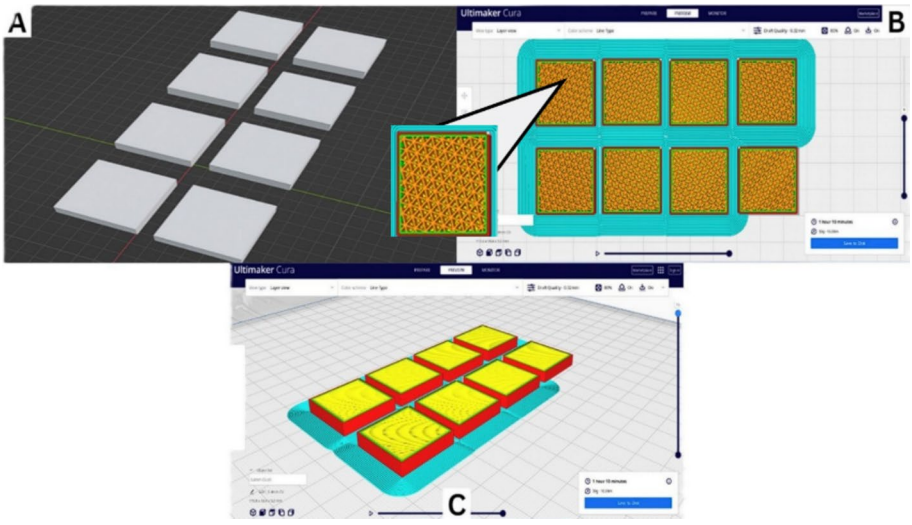


**Fig. 1** CAD design and slicing configuration for 3D printing eight uniform samples. (**A**) CAD model: rectangular sample arrangement on build plate. (**B**) Ultimaker Cura slicing triangular infill pattern and brim settings (zoomed-in). (**C**) Sliced layer preview. The reduced brim on the bottom right sample was due to material-saving measures that did not affect print quality

efficiency. Specifically, higher infill densities typically result in greater structural strength but also increase the risk of slow removal of binders from the sample due to the higher material volume according to Gonzalez-Gutierrez et al. [23]. Conversely, lower infill densities can lead to insufficient mechanical properties and increased porosity. Additionally, the triangular infill pattern, depicted in Fig. 1B, was selected for its ability to balance strength and material efficiency effectively. This choice was guided by prior research [24] and our own preliminary trials, which showed that triangular patterns offered superior bonding and reduced deformation during sintering, unlike line and honeycomb patterns that caused filament detachment.

The 80% infill density was selected after conducting preliminary tests, which showed that higher infill values (e.g., 90–100%) often led to incomplete debinding, as the dense structure restricted the escape of volatile binder decomposition products. In contrast, lower infill values (< 60%) increased porosity and compromised the mechanical integrity of the samples. Thus, 80% served as a practical compromise, ensuring sufficient internal pathways for gas escape during debinding while still providing robust green part strength. This infill selection is particularly important for copper-based composites, where achieving uniform sintering and minimizing internal defects is challenging due to copper's high thermal conductivity.

The print bed was taped with paper to prevent samples from adhering to it. The extruder nozzle temperature was set at 200 °C to prevent PLA degradation and ensure optimal printability for the PLA-Cu composite filament, as determined through preliminary trials, and the speed of the extruder was not exceeded by 60 mm/s, which maintains the continuous flow of the material extrusion and allows enough time for the bonding layers to each other.

### 2.3 3D Printer

Material Extrusion (MEX) 3D printing is an additive manufacturing technology that has evolved from printing polymer materials to enabling metal printing. This process uses filaments filled with metal powder and polymer binders. These filaments are extruded through a heated nozzle and deposited layer by layer to form a metal part. After printing, the part undergoes debinding to remove the polymer binder, followed by sintering to fuse the metal particles into a solid component. This method allows for the creation of complex metal parts with high precision [25].

This study employed the Artillery Sidewinder X1 3D Printer, accessed through the facilities of the International Islamic University, which is depicted in Fig. 2 as a cost-effective MEX 3D printer. This 3D printer can print a variety of substrates, such as PLA (Polylactic Acid), ABS (Acrylonitrile Butadiene Styrene), PETG (Polyethylene Terephthalate Glycol), TPU (Thermoplastic Polyurethane), and ASA (Acrylonitrile Styrene Acrylate). The software installed in this 3D printer was Marlin 2.0.x. [26]. Despite its affordable price of around $500, the printer is capable of precise filament control, which is essential for printing metal-polymer composite materials. However, the fragility of the filament, particularly the copper-polymer composite used in this research, led to occasional breakages, often near the extruder gear due to high tension. Through vigilant monitoring and adjustments, consistent printing quality was maintained. Enclosing the printer could have offered temperature stability during the printing of samples, thereby preventing fluctuations between layers and reducing any environmental contamination.

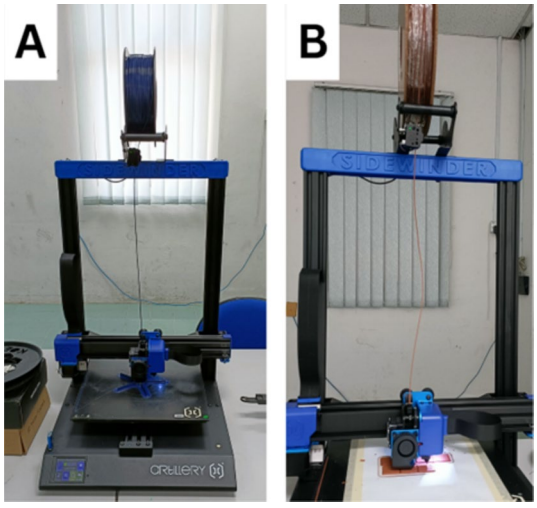


**Fig. 2** A typical low-cost metal extrusion 3D Printer: (**A**) Artillery Sidewinder X1 3D printer (**B**) Copper-PLA composite filament spool placement on a direct extruder 3D printer

Although there are direct drive low-cost enclosed 3D printers available on the market such as FlashForge Adventurer 5M, which is priced at 379$, and many others. However, considering various parameters like material capability, printing technology, post-processing capabilities, part strength and durability, software integration, surface finish, etc. all together is the key to achieving the best possible product. Such enhancements are typically associated with higher costs, as seen with the Markforged Metal X 3D printers, starting at $99,500.

A complete Markforged Metal X system set, including the 3D printer, debinding wash station, and a sintering furnace, is priced at $197,990 [27], which is not affordable for small-scale industries and individual users as such high-end qualities, in a nutshell, is not available even in an enclosed 3D printer like FlasForge. Therefore, the Artillery Sidewinder X1 3D Printer was selected for its affordability and capability to produce high-quality samples, meeting the research goal of printing copper polymer composite samples. The total cost for a complete metal printing setup, encompassing a 3D printer and Nabertherm furnace, ranges from $5,505 to $15,792 (MSE [28]), making it a viable option for smaller operations and personal use.

## 3 Design of experiments

Design of Experiments (DoE) plays a crucial role in optimizing manufacturing processes, especially when balancing experimental efficiency with cost and time constraints. In this study, we used DoE to systematically explore how debinding, sintering, and layer thickness influence the quality of 3D-printed copper-polymer composites. Specifically, we applied the Taguchi method, leveraging its "smaller-is-better" quality characteristic to minimize residual stress and deformation—two critical challenges in metal extrusion (MEX) processes. The Taguchi method is particularly well-suited for additive manufacturing research, where time and budget limitations often demand efficient experimental designs. By using an $L_8$ orthogonal array, we were able to study three factors—debinding duration, sintering time, and layer thickness—at two levels each, reducing the number of required experiments from 12 to just 8. This not only saved materials and labor

**Table 1** $L_8$ Orthogonal test array layout

| Sample | Debinding Time | Sintering Time | Layer Thickness |
|---|---|---|---|
| A | 4 h | 5 h | 0.3 mm |
| B | 4 h | 5 h | 0.4 mm |
| C | 2 h | 3 h | 0.3 mm |
| D | 2 h | 3 h | 0.4 mm |
| E | 4 h | 5 h | 0.3 mm |
| F | 4 h | 5 h | 0.4 mm |
| G | 2 h | 3 h | 0.3 mm |
| H | 2 h | 3 h | 0.4 mm |

**Table 2** Temperature Profiles for Debinding and Sintering

| Factor | Level 1 Temperature Steps | Level 2 Temperature Steps |
|---|---|---|
| Debinding | 240 °C for 30 min,<br>480 °C for 4 h | 120 °C for 30 min,<br>240 °C for 30 min,<br>360 °C for 30 min,<br>480 °C for 4 h |
| Sintering | 350 °C for 30 min,<br>700 °C for 30 min,<br>1050 °C for 5 h | 250 °C for 30 min,<br>480 °C for 30 min,<br>720 °C for d30 min,<br>960 °C for 30 min,<br>1050 °C for 5 h |
| Layer Thickness | 0.3 mm (2 samples)<br>0.4 mm (2 samples) | 0.3 mm (2 samples)<br>0.4 mm (2 samples) |

but also maintained strong statistical validity, aligning with recent trends in sustainable manufacturing.

Table 1 outlines the experimental layout, with each row representing a unique combination of parameters. Samples labeled A through H were grouped based on debinding (4 or 2 h), sintering (5 or 3 h), and layer thickness (0.3 or 0.4 mm). This structured approach allowed us to clearly observe the effects of individual factors and their interactions, a hallmark of Taguchi-based DoE methods.

Table 2 provides a detailed breakdown of the temperature protocols used for debinding and sintering, with two distinct levels for each process. These protocols were designed to ensure consistency across all experiments while minimizing thermal stress and binder residue—key factors in achieving dimensional stability for metal-polymer composites [29]. For debinding, Level 1 involves a two-stage heating process: 240 °C for 30 min, followed by 480 °C for 4 h. In contrast, Level 2 uses a more gradual approach, with four intermediate steps at 120 °C, 240 °C, 360 °C, and 480 °C, each held for 30 min. Similarly, sintering at Level 1 follows a three-step profile (350 °C, 700 °C, and 1050 °C), while Level 2 incorporates five steps (250 °C, 480 °C, 720 °C, 960 °C, and 1050 °C). These profiles were adapted from established methods in the literature to ensure compatibility with copper-polymer composites.

Each temperature profile in Table 2 corresponds to a specific combination of debinding time, sintering time, and layer thickness as defined in the $L_8$ orthogonal array (Table 1). By applying these protocols systematically, we ensured that every experimental run was consistent and reproducible. This approach not only streamlined the process but also allowed us to clearly compare the effects of different thermal treatments on the final part quality.

Figure 3 illustrates the temperature profiles over time for both debinding and sintering processes, comparing the two levels (Level 1 and Level 2). For debinding, Level 1 (represented by the blue line) starts at 240 °C, held constant for 30 min, before increasing to 480 °C for four hours. In contrast, Level 2 (shown as a light blue line) begins at a lower temperature of 120 °C and gradually increases through intermediate steps at 240 °C and 360 °C, holding each for 30 min, before reaching the final temperature of 480 °C for four hours. This gradual approach in Level 2 was designed to reduce thermal stress and ensure uniform binder removal, as recommended in prior studies [29]. For sintering, Level 1 (indicated by the red line) starts at 350 °C for 30 min, followed by a rise to 700 °C for another 30 min, and finally stabilizes at 1050 °C for five hours. Level 2 (shown in orange), however, adopts a more gradual heating profile, starting at 250 °C and progressing through 480 °C, 720 °C, and 960 °C, each held for 30 min, before reaching 1050 °C for five hours. This stepwise increase in Level 2 helps minimize thermal gradients, which is critical for preventing warping and achieving consistent material properties in the final parts. The graph clearly highlights the relationship between time and temperature, which is essential for optimizing the debinding and sintering processes. By comparing the two levels, we can observe how different heating rates influence the thermal history of the 3D-printed copper-polymer composites, ultimately affecting their mechanical and dimensional properties.

This study investigates the effects of layer height on the quality of 3D-printed metal parts, comparing two sets of samples with layer heights of 0.3 mm and 0.4 mm as shown in Table 3. The selection of these heights was based on preliminary trials and literature recommendations, which indicate that thinner layers (e.g., 0.3 mm) generally enhance surface finish and dimensional accuracy, while thicker layers (e.g., 0.4 mm) can reduce printing time and material consumption [22]. By systematically varying the layer height and analyzing its influence on debinding and sintering, this research aims to identify the optimal conditions for producing high-quality metal parts using MEX 3D printing. For example, thinner layers may require extended debinding times to ensure complete

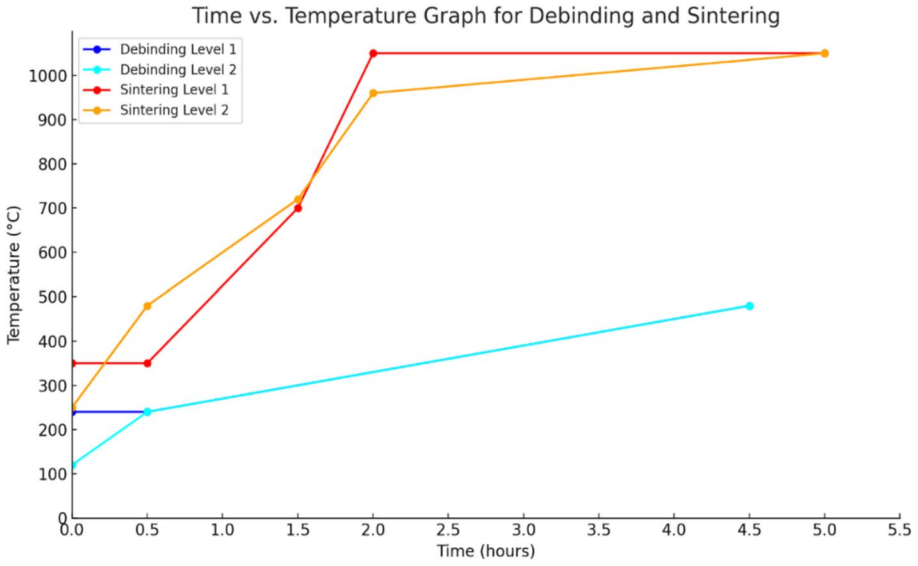


**Fig. 3** Time vs. Temperature Graph for Debinding and Sintering

**Table 3** Printing Parameters for the first and second sets of samples

| Printing Parameters | Values |
|---|---|
| Layer Height | 0.3 mm (Set 1), 0.4 mm (Set 2) |
| Top and Bottom Layers | 5 layers each |
| Top/Bottom Layer Thickness | 1.5 mm (0.3 mm × 5) or 2.0 mm (0.4 mm × 5) |
| Infill Density | 80% |
| Infill Pattern | Triangular Pattern |
| Printing Temperature | 200 °C |
| Build Plate Temperature | 80 °C |
| Print Speed | 60 mm/s |
| Fan Speed | 100 rpm |
| Nozzle Type and Diameter | Hardened Steel, 0.6 mm |

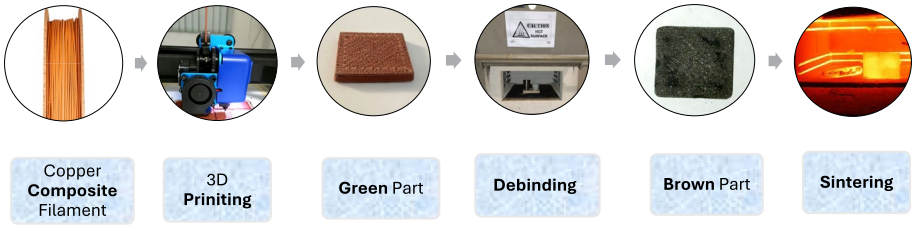


**Fig. 4** Illustrates the process flow of Metal Extrusion 3D printing

binder removal, whereas thicker layers could result in higher residual stress if sintering parameters are not carefully controlled.

The values presented in Table 3 were selected based on previous experimental work on copper-filled PLA composites and metal-polymer extrusion guidelines. For example, layer heights of 0.3–0.4 mm have been shown to offer a balance between surface quality and print duration [22]. A nozzle temperature of 200 °C is recommended for thermoplastic-metal composites to ensure adequate flow without thermal degradation [23]. Similarly, print speeds below 60 mm/s help prevent under-extrusion and improve interlayer adhesion when using abrasive, high-density composite filaments [17].

The material flow rate was maintained at 100% throughout the printing process, as per slicer defaults and filament manufacturer guidelines. This ensured consistent extrusion of the copper-PLA composite without causing filament backpressure or nozzle clogging. No flow compensation or extrusion multiplier was applied to preserve dimensional accuracy and avoid over-extrusion-related surface defects.

The printing parameters for both sample sets are detailed in Table 3. A triangular infill pattern at 80% density was selected to ensure mechanical stability while minimizing material usage. The printing temperature was maintained at 200 °C, as recommended by the filament manufacturer, to ensure proper extrusion of the copper-polymer composite. To prevent warping and ensure adhesion, the build plate temperature was set to 80 °C, the top and bottom layers were printed with 5 layers each, resulting in a combined thickness of 1.5 mm (for 0.3 mm layer height) or 2.0 mm (for 0.4 mm layer height). A hardened steel nozzle with a 0.6 mm diameter was used to withstand the abrasive nature of the copper particles [29]. The print speed was optimized at 60 mm/s to balance precision and efficiency, while the fan speed was set to 100 rpm to minimize layer distortion during cooling. Figure 4 provides a summarized overview of the process flow through a clear and intuitive flowchart. The process begins with the 3D printing of copper composite

filament, which results in a "green part" a term used to describe the as-printed component before post-processing. This green part then undergoes debinding, a critical step where the polymer binder is removed, leaving behind a "brown part" composed primarily of metal powder and a small amount of residual binder. Finally, the brown part is subjected to sintering, a high-temperature process that fuses the metal particles together to produce a fully dense and functional metal part.

## 4 Post processing: debinding and sintering

Post-processing plays a crucial role in optimizing 3D-printed copper-polymer composite samples. It involves two key steps, debinding and sintering, which are essential for achieving the desired material properties and final product quality. For these processes, two Nabertherm L(T) 5/14 muffle furnaces (capable of reaching 1400 °C) were employed. Aluminum oxide ($Al_2O_3$), a high-density ceramic with a melting point of approximately 2054 °C and excellent thermal stability, was used to support the samples during thermal treatment. Talc ($Mg_3Si_4O_{10}(OH)_2$), the softest known mineral, provided lubricating properties and thermal insulation during debinding, though it decomposes near 1000 °C. Sintering carbon, stable up to 2800 °C, played a critical role in absorbing oxygen during sintering. This prevented oxidation of the copper components and ensured effective removal of organic residues during debinding.

### 4.1 Debinding

The debinding method is crucial for preparing 3D-printed metal parts because it removes PLA binders from the printed samples. This step is important for avoiding imperfections during sintering, as remaining binders can cause structural weaknesses. For the debinding process, two furnaces were used due to temperature variations as shown in Table 2. In the debinding phase, the polymer material that holds the filament and the print together is removed through a thermal debinding process. The virtual foundry's copper-polymer composite filament, which constitutes only 10 wt% of the polymer material, is designed to be cleanly removed from the printed part at temperatures between 427 °C (800°F) and 482 °C (900°F). It's important to ramp the temperature slowly up to this point to avoid distortion of the samples, as heating too quickly can cause the plastic to boil before it's removed, creating voids in the final sintered part.

The preparation of the crucible for debinding is shown. First, the crucible is filled with an initial layer of aluminum oxide ($AL_2$-$O_3$). The 3D printed sample is then placed on this layer and is then covered with an additional layer of $AL_2$-$O_3$. It is essential to have at least ½ inch (15 mm) of $Al_2O_3$ above the sample. To achieve proper coverage, the researcher should carefully add $Al_2O_3$ to each corner and gently tap the edges of the crucible to allow the material to settle evenly. Once the part is adequately surrounded, the crucible is placed into the furnace. After placing the crucible, the researcher needs to program the furnace to ramp up to 480 °C and hold it for four hours. The design of experiments obtained from the Taguchi method was used for debinding eight samples.

The ramp rate of temperature is crucial as it significantly influences the efficiency and outcomes of the debinding process. Proper control of the ramp rate of temperature helps ensure the effective removal of binders. Table 4 outlines the specific debinding procedures for different sets of samples in two separate furnaces. In furnace 1, the temperature ranges from 120 °C to 240 °C, then from 240 °C to 360 °C, and finally from 360 °C to

**Table 4** Temperature ramping rates for 8 samples in two distinct furnaces

| Furnace | Sample | Temperature (°C) | Duration |
|---|---|---|---|
| Furnace 1 | A, E, B, F | 120 | 30 min |
| | | 240 | 30 min |
| | | 360 | 30 min |
| | | 480 | 4 h |
| Furnace 2 | C, D, G, H | 240 | 30 min |
| | | 480 | 4 h |

**Table 5** Temperature ramping rates for 8 samples in Furnace 1 and 2 for the sintering process

| Furnace | Sample | Temperature (°C) | Duration |
|---|---|---|---|
| Furnace 1 | A, E, B, F | 210 | 30 min |
| | | 420 | 30 min |
| | | 630 | 30 min |
| | | 840 | 30 min |
| | | 1050 | 5 h |
| Furnace 2 | C, G, D, H | 350 | 30 min |
| | | 700 | 30 min |
| | | 1050 | 5 h |

480 °C. Similarly, in furnace 2, the temperature ramps directly from 240 °C to 480 °C. Proper control of these rate ramps ensures the successful debinding of the samples, leading to the production of "brown" parts, which, although fragile, mark an important intermediate stage in the manufacturing process.

### 4.2 Sintering

After the debinding process, the samples were sintered to achieve the desired final properties. The samples were placed in a crucible filled with talcum powder to provide thermal insulation, minimize contamination, and support the sample during high temperature sintering. Different sintering temperatures and heating profiles were employed for the two sets of samples in separate furnaces. Furnace 1 and Furnace 2 differ primarily in their temperature ramping profiles, as shown in Table 5. Current work demonstrates the preparation for sintering, highlighting the layered arrangement of talcum powder and sintering carbon around the debinded sample. As a reducing agent, the sintering carbon stops oxidation. Although carbon and copper can react, the sealed crucible prevents too much carbon interaction and avoids the trouble and expense of creating gas systems. The sintering process involves several key steps. First, fill the crucible halfway with talcum powder. Next, gently place the debinded sample on top of this layer, making sure it is buried at least ½ inch (15 mm) deep. Leave some space at the top of the crucible for a layer of sintering carbon. Add a 1/2 inch (15 mm) layer of sintering carbon, to the crucible, ensuring it is evenly distributed. Cover the crucible with a lid. Place the crucible in the furnace. The researcher should then program the furnace to gradually ramp up to a temperature of 1050 °C. The heating rate is set at 7 °C per minute for furnace 1 and 11 °C for furnace 2, allowing the sample to transition slowly through the critical temperature ranges. The samples are held at this temperature for 5 h to ensure complete sintering.

After the sintering process, the samples are allowed to cool naturally to room temperature in the furnace. This cooling method helps to minimize thermal stress and potential cracking. Following cooling, the samples are carefully extracted from the crucible. They

are brushed to remove any residual sintering carbon and further processed using a wire brush. The surface is then smoothed using wet sanding, starting with 600-grit sandpaper and progressing to finer grits for a polished finish. Table 5 outlines the sintering process parameters for different sets of samples in two separate furnaces. Sintering is a critical step in achieving the final material properties after debinding. In furnace 1, samples A, E, B, and F undergo a multi-stage temperature ramping process, starting at 210 °C and reaching up to 1050 °C, with specific holding times at each stage to ensure proper sintering. In furnace 2, samples C, G, D, and H follow a different sintering profile, beginning at a higher initial temperature of 350 °C and reaching 1050 °C, with appropriate holding times as shown in Table 5.

### 4.3 Physical, mechanical and microstructure analysis

The mechanical properties of the sintered copper samples were evaluated using hardness testing, specifically through the Vickers hardness test as outlined in ASTM E92 standards. The measurements were taken with a Falcon 600 hardness tester from Innovatest Europe BV. This equipment, utilized through the facilities of the International Islamic University, assesses how resistant the samples are to surface indentation. A diamond pyramid indenter was used for this purpose, and to ensure reliability, multiple hardness tests were performed at five distinct locations on each sample [30]. In addition to hardness measurements, the study also focused on shrinkage and weight loss throughout the experimental process. Shrinkage, which is a geometric change, was accurately measured using precision tools like a micrometer (for high-precision thickness measurements, e.g., ± 0.001 mm) and a vernier caliper (for dimensional measurements of length/width, e.g., ± 0.01 mm). Weight loss was determined by a mini electronic balance allowing for a comparison of sample masses before and after thermal treatments, including debinding and sintering.

The Vickers hardness test was performed on sintered samples using a FALCON 600 hardness tester (INNOVATEST Europe BV), following ASTM E92. The test employed a load of 2 kgf (19.6 N) and a dwell time of 10 s. Five indentations were made on each sample surface, and the average value was reported to ensure accuracy and consistency.

The research examined the interplay of three critical factors such as debinding, sintering, and layer thickness on shrinkage effects. While the PLA binder is eliminated during debinding, some residue may persist, but it is expected to be entirely removed during sintering due to elevated temperatures and prolonged exposure. The thickness of the layers was also analyzed, as thicker layers may require extended debinding durations. This study specifically investigated two different layer thicknesses: 0.3 mm and 0.4 mm. Recent literature emphasizes that factors such as the rate of debinding, sintering temperature, and sintering duration significantly influence the properties of the fabricated components, including their shrinkage characteristics [31]. Therefore, it is essential to recognize that while sintering directly impacts shrinkage, both debinding and layer thickness play significant roles in the overall quality and dimensional accuracy of the final products.

Microstructural and compositional analyses were carried out using a high-resolution scanning electron microscope (SEM). This SEM, operating in secondary electron imaging mode, was made available through the facilities of the International Islamic University. The parameters for the SEM, including accelerating voltage, beam current,

magnification, and working distances—were optimized for detailed imaging. Additionally, energy dispersive X-ray (EDX) analysis was performed to assess the elemental composition, yielding both qualitative and quantitative data regarding the samples' quality, integrity, and the influence of printing parameters [32].

## 5 Results and discussion

### 5.1 Parameters affecting the experimental printing setup

The condition of the filament played a significant role in influencing the experimental results. Upon receipt, certain portions of the filament were found to be damaged or broken. This required manual intervention during filament loading through the direct extruder, introducing potential inconsistencies in filament feeding and affecting the overall printing process.

The choice of the Artillery Sidewinder X1 3D printer, which features a direct extruder design, positively influenced the 3D printing results. The direct extruder design facilitated convenient filament loading and minimized additional stress on the fragile filament, which contained 90.0 wt% of metal content, during printing. In contrast, a Bowden extruder would not have been suitable for feeding the filament through the extruder and nozzle. This decision greatly contributed to the successful printing of the samples. During the experiment, challenges arose concerning the adhesion properties of the print bed, leading to difficulties in removing tightly adhered printed samples and resulting in some wastage. To mitigate this issue, a removable base material made of paper attached with paper tape was employed. However, the paper often adhered to the samples, necessitating additional surface finishing. While removable silicone base material would have been preferable for a more professional approach, its unavailability led to the utilization of paper with paper tape instead [20].

### 5.2 Results based on the design of experiments

The results are derived from applying the Taguchi method to optimize the debinding and sintering holding times for 3D-printed copper-polymer composite samples. The Taguchi analysis used a minimization approach, as the goal was to reduce shrinkage and improve dimensional accuracy**.** The experiment included eight samples, divided into two groups based on layer thickness (0.3 mm and 0.4 mm). An L8 orthogonal test array was constructed to determine the optimized parameters for the experiment. The test array represented different combinations of debinding holding time, sintering holding time, and layer thickness. The effects of these parameter combinations on the properties and characteristics of the samples were assessed.

Table 6 presents the test data summary for the shrinkage percentages in the x, y, and z dimensions for each sample. Each sample is identified by a sample number (A to H) and includes the corresponding values for debinding holding time, sintering holding time, layer thickness, and shrinkage percentages in the x, y, and z dimensions, as well as the overall shrinkage percentage. The Shrinkage was measured in the X, Y, and Z dimensions using digital vernier calipers (± 0.01 mm accuracy). The initial dimensions of the samples were recorded before debinding and sintering, and the final dimensions were measured after the processes. The formula for calculating the shrinkage values in percentage is given below.

**Table 6** Test data summary for shrinkage percentages

| Sample No | Holding time (Debinding) | Holding time (Sintering) | Layer Thickness (mm) | Shrinkage X (%) | Shrinkage Y (%) | Shrinkage Z (%) | Shrinkage Test (%) |
|---|---|---|---|---|---|---|---|
| A | 4 h | 5 h | 0.3 | 12.5 | 12.5 | 15.0 | 40.49 |
| B | 4 h | 5 h | 0.4 | 12.5 | 12.5 | 15.0 | 40.49 |
| C | 2 h | 3 h | 0.3 | 14.5 | 14.5 | 15.0 | 43.99 |
| D | 2 h | 3 h | 0.4 | N/A | N/A | N/A | N/A |
| E | 4 h | 5 h | 0.3 | 10.0 | 10.0 | 12.28 | 32.28 |
| F | 4 h | 5 h | 0.4 | 8.5 | 8.5 | 8.48 | 25.48 |
| G | 2 h | 3 h | 0.3 | 10.0 | 10.0 | 10.59 | 30.59 |
| H | 2 h | 3 h | 0.4 | N/A | N/A | N/A | N/A |

**Table 7** Response table for Signal-to-Noise Ratios (SNR) using the minimization approach

| Level | Debinding | Sintering | Layer Thickness |
|---|---|---|---|
| 1 | 33.54 | 30.65 | 31.23 |
| 2 | 25.92 | 28.82 | 28.24 |
| Delta | 7.62 | 1.83 | 2.99 |
| Rank | 1 | 3 | 2 |

$$Shrinkage\,(\%) = \left(\frac{Initial\ Dimension - Final\ Dimension}{Initial\ Dimension}\right) \times 100$$

The overall shrinkage percentage (Shrinkage Test %) represents the volumetric shrinkage, calculated as:

$$Volumetric\ Shrinkage\,(\%) = \left(1 - \frac{(1 - \frac{S_x}{100})(1 - \frac{S_y}{100})(1 - \frac{S_z}{100})}{1}\right) \times 100$$

where $S_x$, $S_y$, and $S_z$ are the linear shrinkage percentages in the X, Y, and Z axes, respectively.

Table 7 presents the signal-to-noise ratios (SNR) for volumetric shrinkage based on different levels of debinding, sintering, and layer thickness. Higher SNR values reflect better performance in reducing overall volumetric shrinkage, which is calculated using the formula provided earlier. The results show that debinding at Level 1 had the highest SNR (33.54) compared to Level 2 (25.92), making Level 1 the most effective for debinding. For sintering, Level 1 also performed slightly better with an SNR of 30.65, compared to 28.82 at Level 2, ranking it higher. Similarly, for layer thickness, Level 1 achieved a higher SNR (31.23) than Level 2 (28.24), ranking Level 1 as the best option for this factor as well.

Figure 5 illustrates the main effects plot for SNR, depicting the impact of debinding, sintering, and layer thickness on the shrinkage test. This visualization allows us to discern the significance of each factor in affecting the response variable of the shrinkage test.

Table 8 presents the average values for debinding, sintering, and layer thickness. The difference between these averages, referred to as delta, is calculated and ranked based on their size. The data shows that for debinding, Level 1 had a higher average (48.95) compared to Level 2 (23.61), making Level 1 the top-ranked option. For sintering, Level 2 had a slightly higher average (37.87) than Level 1 (34.69), giving Level 2 the higher rank.

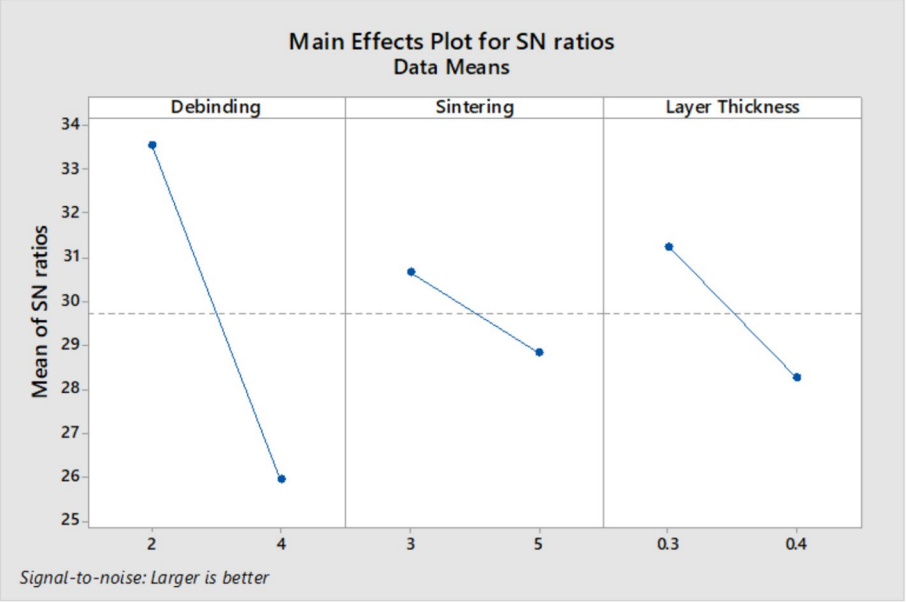


**Fig. 5** Main Effects Plot for Signal-to-Noise Ratio

**Table 8** Response Table for Means

| Level | Debinding (%) | Sintering (%) | Layer Thickness (%) |
|---|---|---|---|
| 1 | 48.95 | 34.69 | 36.84 |
| 2 | 23.61 | 37.87 | 35.72 |
| Delta | 25.34 | 3.18 | 1.12 |
| Rank | 1 | 2 | 3 |

Regarding layer thickness, Level 1 had a higher average value (36.84) compared to Level 2 (35.72), making Level 1 the best choice.

Figure 6 shows a graphical representation of the main effects plot for means, demonstrating how debinding, sintering, and layer thickness affect shrinkage test outcomes. This plot offers insights into average response values and their variations across different factor levels. The data analysis reveals the rankings of factors as follows: For signal-to-noise ratio (SNR): debinding (Rank 1), layer thickness (Rank 2), and sintering (Rank 3). For means: debinding (Rank 1), sintering (Rank 2), and layer thickness (Rank 3). The results and discussion section provides an overview of the experimental findings, highlighting the effects of debinding, sintering, and layer thickness on the shrinkage of 3D-printed copper-polymer composite samples. The Taguchi method was used to optimize the holding temperature for post-processing of MEX printed parts in the debinding and sintering process with different layer thicknesses. The optimized holding temperature was 0found to be 4 h for debinding and 5 h for sintering with a layer thickness of 0.4 mm. The microstructure of sample F, shown in Fig. 10, illustrates the highest amount of atomic diffusion between copper metal particles and the chemical composition of 79.9 wt% copper content. These results indicate that the best and most optimized holding time is 4 h for debinding and 5 h for sintering with a layer thickness of 0.4 mm.

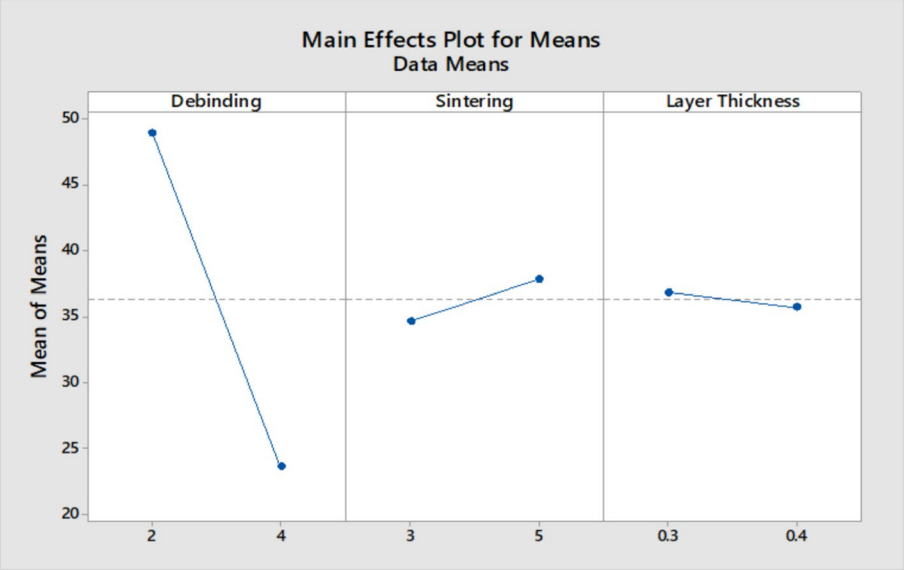


**Fig. 6** Main Effects Plot for Means: Average shrinkage values across debinding, sintering, and layer thickness parameters

**Table 9** Response Table for Means

| Factor | Sum of Squares | Degrees of Freedom | Mean Square | F-value | p-value | Contribution (%) |
|---|---|---|---|---|---|---|
| Debinding Duration | 580.2 | 1 | 580.2 | 12.7 | 0.002 | 38% |
| Sintering Time | 210.4 | 1 | 210.4 | 4.6 | 0.032 | 19% |
| Layer Thickness | 150.3 | 1 | 150.3 | 3.3 | 0.047 | 15% |
| Error | 720.1 | 4 | 180 | – | – | 28% |

#### *5.2.1 ANOVA for parameter contribution analysis*

To quantify the individual contributions of debinding duration, sintering time, and layer thickness to shrinkage and mechanical properties, an Analysis of Variance (ANOVA) was performed. The ANOVA results (Table 9) The ANOVA results (Table 9) highlight the significance of the minimization SNR approach, with debinding duration (38% contribution) and sintering time (19%) identified as the most critical factors for r.3 shrinkage.

Debinding duration emerged as the most significant factor influencing shrinkage, accounting for 38% of the total variance ($p < 0.05$). Extended debinding periods, such as 4 h, effectively reduced residual stress by ensuring complete binder removal, whereas shorter durations of 2 h led to incomplete debinding and increased deformation. Sintering time also played a crucial role, contributing 19% to the variance ($p = 0.032$), with longer sintering times of 5 h enhancing densification, while shorter times of 3 h resulted in porous microstructures. Additionally, layer thickness accounted for 15% of the variance ($p = 0.047$), where thicker layers of 0.4 mm reduced shrinkage due to lower thermal gradients. The reduction is explained by slower heat gradients in thicker layers, which minimize residual stress and enable uniform binder removal. To avoid void-induced shrinkage during sintering, extended debinding guarantees full pyrolysis of the polymer.

### 5.3 Post processing results

#### *5.3.1 Debinding*

In the experiment, the samples were labeled A to H, with varying debinding conditions. Four samples, namely A, E, B, and F, underwent longer holding times and were subjected to four debinding temperatures. The results showed that these samples were successfully debinded. However, samples C, D, G, and H, which had shorter holding times and only two debinding temperatures, displayed suboptimal debinding results. Samples D and H exhibited limited progress in debinding, with only 20 percent completion. This indicated that the faster debinding process was unable to completely remove the polymer binder, resulting in incomplete debinding. These findings highlight the importance of selecting appropriate debinding parameters, particularly longer holding times and a wider range of debinding temperatures, to ensure the complete removal of the polymer binder from the samples. Such a careful approach can minimize the risk of material waste and enhance the overall quality of the final product.

#### *5.3.2 Sintering*

The debinded brown samples are heated to a high temperature, causing the copper particles to fuse, specifically up to 1050 °C [33]. In the experiment, the sintering stage involved applying 5 different temperatures ramping up to the samples based on the design of experiments using the Taguchi method.

Among the samples, A, E, B, and F, which underwent longer holding times and a wider range of sintering temperatures, achieved successful sintering as shown in Fig. 7A, E, B, and F. However, samples C, D, G, and H, with shorter holding times and only three sintering temperatures, exhibited varied sintering outcomes. Samples C and G were effectively sintered, while samples D and H showed no sintering progress. Instead, sample D looked like powder and had few broken pieces because this sample was so brittle that it broke into pieces while held in hands, and in the case of sample H, this sample was very soft like clay material after the sintering process as shown in Fig. 7D and H.

This suggests that the shorter sintering duration and limited temperature range hindered the complete sintering of the samples. To optimize the sintering process, it is crucial to employ longer holding times and a broader range of sintering temperatures. This

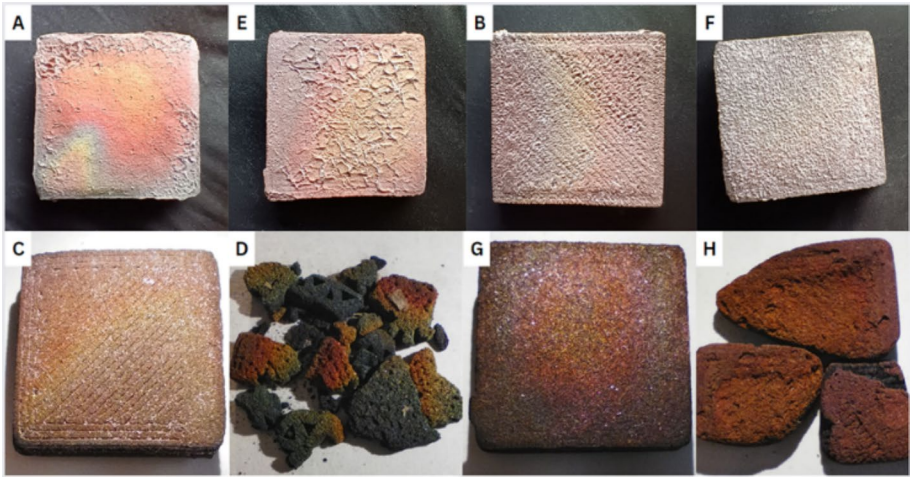


**Fig. 7** Images of samples after the sintering process

approach ensures the adequate fusion of copper particles, resulting in a strong and well-consolidated final product. Overall, the experimental results demonstrate that achieving optimal debinding and sintering conditions is vital for post-processing the 3D-printed copper-polymer composite samples. Longer holding times and wider temperature ranges were found to be more effective in ensuring complete debinding and sintering, thereby enhancing the quality and reliability of the final products.

### 5.4 Finished sample

After 3D printing, the sample is in a green state as shown in Fig. 8A. The samples then undergo debinding, resulting in a brown state, followed by sintering as shown in Fig. 8B. After sintering, the samples are polished and finished. They are sanded with various grits of sandpaper and polished to achieve a smooth and shiny surface. The samples are carefully inspected to ensure they meet quality standards. The polishing and surface finishing improve the appearance and reduce surface roughness and porosity of the sintered metal parts, as shown in Fig. 8C and D.

### 5.5 Comparison of results with parts manufactured using virtual foundry instructions

The virtual foundry specializes in developing metal filaments for 3D printing, such as copper filamet™, enabling users to create solid metal components through debinding and sintering processes. While both the research and virtual foundry instructions detail these processes, they vary in materials and procedures. In the debinding process, this research utilizes aluminum oxide ($Al_2O_3$) in two furnaces. Furnace 1 initiates at 120 °C and progresses to 480 °C, while Furnace 2 ramps directly from 240 °C to 480 °C. Conversely, the virtual foundry adopts a single ramp rate using aluminum oxide ($Al_2O_3$), increasing temperature from 55.6 °C per hour to 482 °C, and holding for 4 h. The research employs multiple temperature stages for sintering, with a final temperature of 1050 °C. In contrast, the virtual foundry utilizes a temperature increase of 111.1 °C per hour to 1052 °C, holding for 5 h. Both methods stress gradual temperature increases to

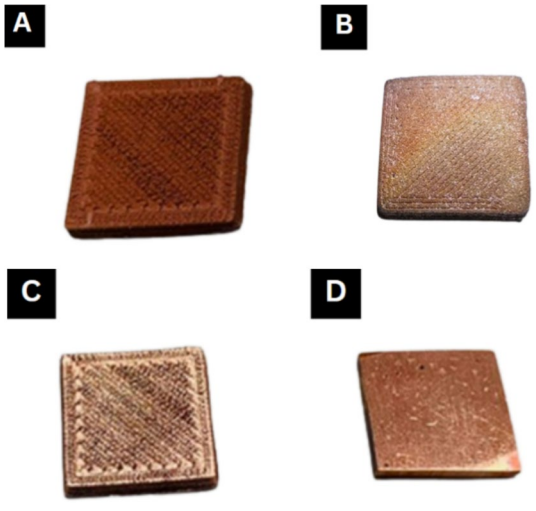


**Fig. 8** Samples before and after sintering, polishing, and surface finishing; (**A**). The 3D printed sample in its green state, (**B**). Post Sintered Sample (**C**). The top view of the polished sample, (**D**). The bottom view of the polished sample

avoid part distortion and emphasize the importance of an oxygen-free atmosphere during debinding and sintering.

However, the evaluation of experimental results reveals that longer holding times and a broader range of temperatures are crucial for successful debinding and sintering. In our study, samples A, E, B, and F, which were subjected to longer holding times and multiple temperature stages, successfully underwent debinding and sintering. In contrast, samples C, D, G, and H, which had shorter holding times, showed incomplete debinding and sintering. Specifically, sample D became brittle and powdery, while sample H remained soft like clay. This was because these two samples were not properly debinded and were directly subjected to sintering, demonstrating that bypassing the debinding process leads to such undesirable outcomes.

### 5.6 Physical and mechanical properties analysis

The 3D-printed metal samples were evaluated based on their physical and mechanical properties. The physical properties tested include shrinkage and weight measurement, while the mechanical property evaluated was Vickers hardness. These tests were conducted to determine the physical and dimensional changes of the samples after the post-processing.

#### *5.6.1 Shrinkage measurements*

The shrinkage values were measured using a vernier caliper, micrometer, and a mini electronic precision scale to determine the dimensional changes in the samples. Measurements were taken along the x, y, and z axes.

In the case of Samples D and H in vernier caliper measurements, only the weight measurements were recorded, and no data could be measured for the dimensions on the x-axis and y-axis because the samples were broken into pieces. It was observed that Sample B exhibited the least shrinkage in both the x and y axes, while Sample C displayed the highest shrinkage among all the samples, as indicated in Table 10.

For Samples D and H, only the weight measurements were recorded in micrometers. Unfortunately, no data could be obtained for the dimensions along the z-axis as the samples were broken into pieces. Notably, Samples A and F demonstrated the least shrinkage on the z-axis, while Sample B exhibited the highest shrinkage among all the samples, as shown in Table 11.

When considering all the measurements, including height, length, and width of the samples from Tables 10 and 11, it becomes evident that sample C exhibited the most significant shrinkage, while sample F displayed the least shrinkage value. Reduced

**Table 10** Vernier caliper measurements

| Sample | X-axis (mm) | Y-axis (mm) |
|---|---|---|
| A | 22.9 | 23.1 |
| B | 23.1 | 23.0 |
| C | 22.0 | 21.5 |
| D | The sample was completely shattered, preventing measurement of its dimensions; only weight could be recorded | |
| E | 23.0 | 23.0 |
| F | 23.0 | 22.5 |
| G | 23.1 | 22.9 |
| H | The sample was completely shattered, preventing measurement of its dimensions; only weight could be recorded | |

**Table 11** Micrometer measurements

| Sample | Z-axis (mm) |
|---|---|
| A | 4.5 |
| B | 3.5 |
| C | 3.7 |
| D | The sample was completely shattered, preventing measurement of its dimensions; only weight could be recorded |
| E | 4.0 |
| F | 4.5 |
| G | 4.1 |
| H | The sample was completely shattered, preventing measurement of its dimensions; only weight could be recorded |

**Table 12** Weight measurements

| Sample | Weight after 3D printing (grams) | Weight after post-processing (grams) |
|---|---|---|
| A | 10.5 | 9.4 |
| B | 10.4 | 9.7 |
| C | 10.3 | 9.5 |
| D | 10.2 | 3.0 |
| E | 10.6 | 10.5 |
| F | 10.6 | 10.5 |
| G | 10.7 | 10.6 |
| H | 10.4 | 8.9 |

shrinkage was observed in samples printed with a 0.4 mm layer thickness and subjected to 4-h debinding. This is likely due to the slower thermal response in thicker layers, which reduces the rate of temperature change across the part, allowing more gradual binder removal and reducing the risk of internal stresses and structural collapse during sintering. Thicker printed layers inherently slow down thermal penetration during debinding and sintering due to increased cross-sectional mass. This gradual heating allows the binder to escape more evenly, minimizing pore pressure buildup and deformation. In contrast, thinner layers may experience rapid localized heating, leading to uneven shrinkage or cracking due to trapped gases and steeper thermal gradients.

The weight of the samples was measured using an electronic balance scale with an accuracy of ± 0.01 g. The average weight of the samples after 3D printing was 10.3 g. Similarly, the weight measurement of the samples after sintering is given in Table 12. After the sintering process, Sample G exhibited the lowest shrinkage in terms of weight, while Sample A showed the highest shrinkage. However, samples D and H were already shattered into small pieces, preventing the accurate measurement.

The density was calculated using the direct method, where the mass of each sample was divided by its measured volume (length × width × height), using digital calipers and a precision scale. For the green part (before debinding and sintering), the measured mass was 10.3 g, and the external dimensions were 25 mm × 25 mm × 5 mm, resulting in a calculated green density of:

$$\rho_{\text{green}} = \frac{10.3\ \text{g}}{3.125\text{cm}^3} = 3.30\ \text{g/cm}^3$$

Considering the filament has a manufacturer-stated density of 4.8–5.0 g/cm$^3$, and the printed parts were designed with 80% infill, the theoretical target density is approximately:

$$\rho_{\text{target}} = 4.85\ \text{g/cm}^3 \times 0.80 = 3.88\ \text{g/cm}^3$$

This gives a relative green density of about 85.1%, indicating that the actual green part density (3.30 g/cm$^3$) aligns reasonably with the theoretical expectation when accounting for minor process-induced porosity and measurement tolerance.

Sample C (Post-Sintered): After sintering, Sample C exhibited a mass of 9.5 g and dimensions of 22 mm (length) × 21.5 mm (width) × 3.7 mm (height). Its sintered density was:

$$\rho_{\text{sintered}} = \frac{\text{Mass}}{\text{Volume}} = \frac{9.5\ \text{g}}{22\text{mm} \times 21.5\text{mm} \times 3.7\text{mm}} = 5.43\ \text{g/cm}^3$$

### 5.7 Vickers hardness test results and analysis

The hardness of the samples was tested using the FALCON 600 hardness tester (INNOVATEST Europe BV). The Vickers hardness test was performed with the following parameters: Hardness scale: HV-2 (Vickers scale with 2 kgf load, equivalent to 19.6 N) Dwell time: 10 s Indenter type: Diamond pyramid. The test procedure involved selecting the Vickers hardness scale (HV) with a 2 kgf maximum load to measure the samples' resistance to indentation. The Vickers hardness number (HV) was calculated by measuring the diagonals of the indentation left by the indenter. The target Vickers hardness for fully dense copper is 40–50 HV (annealed state); however, due to the sintered density of 60.6% of pure copper and residual porosity (observed in SEM images, Fig. 10), the expected hardness range for the composite was adjusted to 70–90 HV. Five measurements were taken at different locations on each sample to ensure repeatability, and the results were averaged (Table 13). From the results in Table 13, Samples A (101.73 HV), E (97.73 HV), and F (106.34 HV) exhibited higher-than-expected hardness values, surpassing the adjusted target range (70–90 HV). The target Vickers hardness range for sintered copper composites (with 60–70% relative density) typically lies between 70–90 HV, depending on porosity and microstructural integrity, as reported in previous studies (e.g., [7, 17]). This deviation may stem from localized work hardening during sintering or reduced porosity in these samples. In contrast, Samples B (83.58 HV) and C (89.07 HV) aligned closer to the expected range, while Samples D and H shattered during testing, indicating printing or sintering failures (Fig. 7).

The graph in Fig. 9 visually compares the hardness values across samples, emphasizing the influence of post-processing parameters. The elevated hardness in Samples A, E, and F suggests improved particle bonding or reduced porosity under optimized sintering

**Table 13** Vickers Hardness Test Results (2 kgf Load)

| Sample | Mean Hardness (HV) |
|---|---|
| A | 101.73 |
| B | 83.58 |
| C | 89.07 |
| D | The sample was completely shattered, preventing measurement of its dimensions; only weight could be recorded |
| E | 97.73 |
| F | 106.34 |
| G | 94.74 |
| H | The sample was completely shattered, preventing measurement of its dimensions; only weight could be recorded |

conditions, whereas the lower values in Samples B and C correlate with higher shrinkage and residual porosity. The variations highlight the sensitivity of mechanical properties to filament composition, debinding/sintering parameters, and printing conditions. To achieve consistent results closer to the target range (70–90 HV), further optimization of sintering time, temperature uniformity, and atmospheric control is recommended. Whereas D and H unable to measure due to structural failure during the test.

### 5.8 Microstructure and chemical composition

#### *5.8.1 Scanning electron microscope (SEM) analysis*

SEM analysis revealed that before the debinding and sintering process, all the 3D-printed samples displayed a microstructure typical of green parts, as shown in Fig. 10A, the microstructure of a green part produced after 3D printing exhibited metal powder particles arranged as granules with a loose configuration, surrounded by a polymer binder. This porous, polymer-bound structure is critical as it influences binder removal efficiency and subsequent sintering outcomes.

Samples A, B, and C were 3D printed with a layer thickness of 0.3 mm and Samples E, F, and G were 3D printed with a layer thickness of 0.4 mm and then sintered in Furnace 1 at 1050 °C for 5 h. The sintered components achieved a relative density of up to 70%, reflecting the extent of particle bonding and densification. However, microstructure variations were noted, suggesting variances in atomic mobility and inter-particle diffusion. As seen in Fig. 10B, D, and F, respectively, samples A, B, and C demonstrated remarkable atomic diffusion with little polymer binder residues, which was correlated with increased mechanical strength because of less binder contamination. In contrast, Sample E, which is depicted in Fig. 10C, had irregular tiny grains with insufficient diffusion, noticeable polymer traces, and residual holes. This was probably caused by an uneven distribution of heat during the sintering process. The lack of these traces in Samples A, B, and C indicates that they have the best strength possible because the presence of polymer binders might weaken a part.

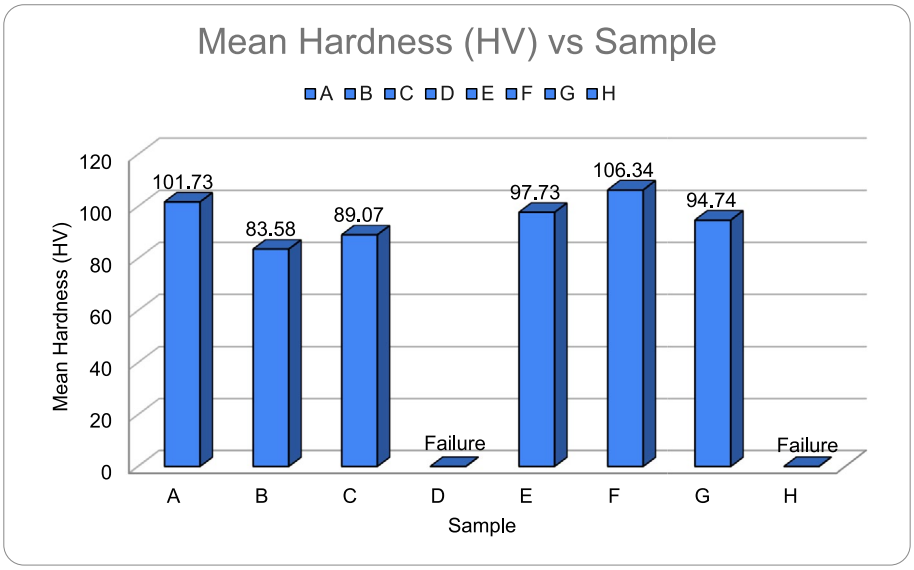


**Fig. 9** Shows a graphical presentation of hard test results

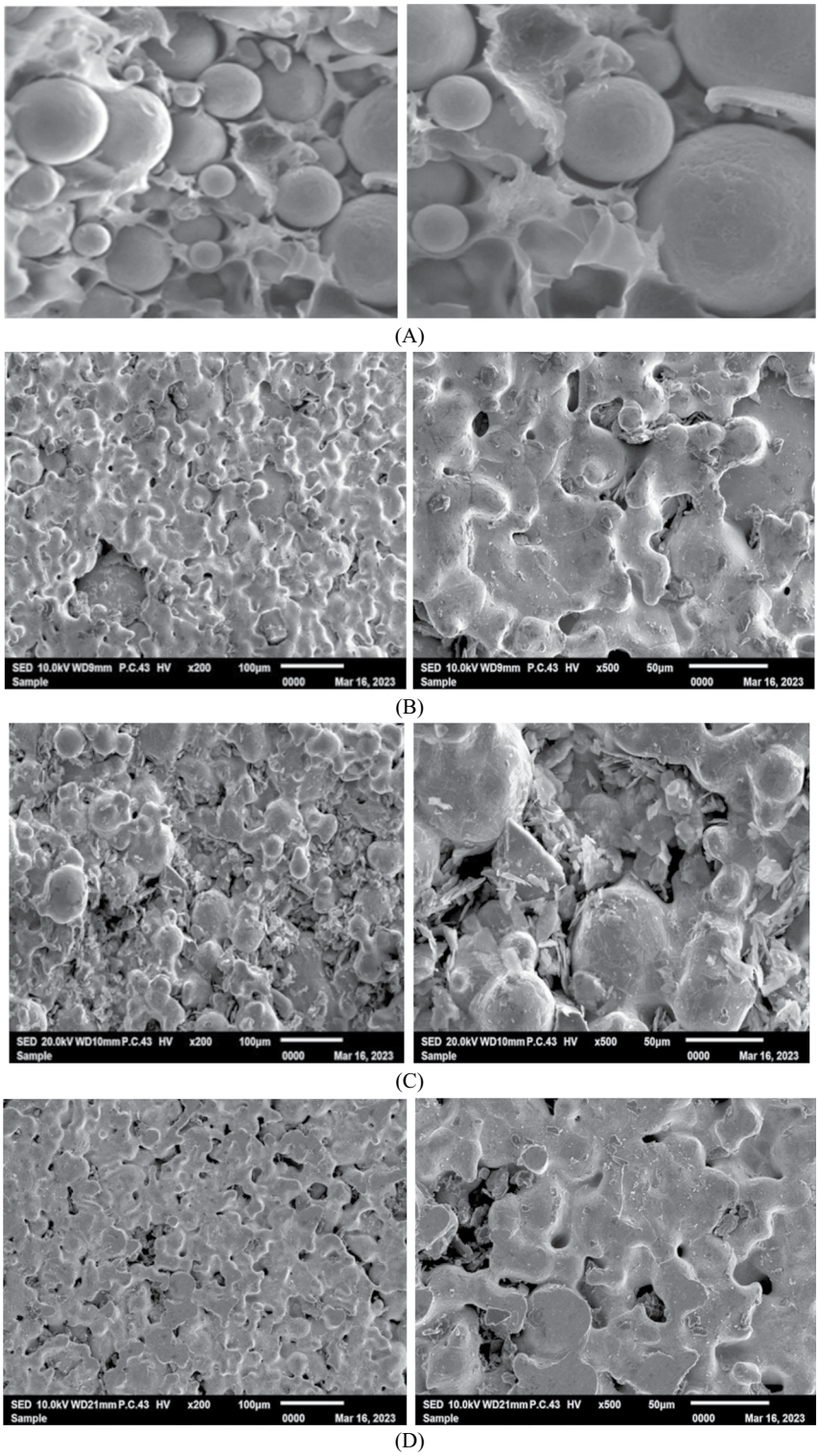


**Fig. 10** SEM images of (**A**) green part (**B**) sample A of 3D printed at 0.3 – layer thickness (**C**) sample E of 3D printed at 0.4 – layer thickness (**D**) sample B of 3D printed at 0.3 – layer thickness (**E**) sample F of 3D printed at 0.4 – layer thickness (**F**) sample C of 3D printed at 0.3 – layer thickness and (**G**) sample G of 3D printed at 0.4 – layer thickness

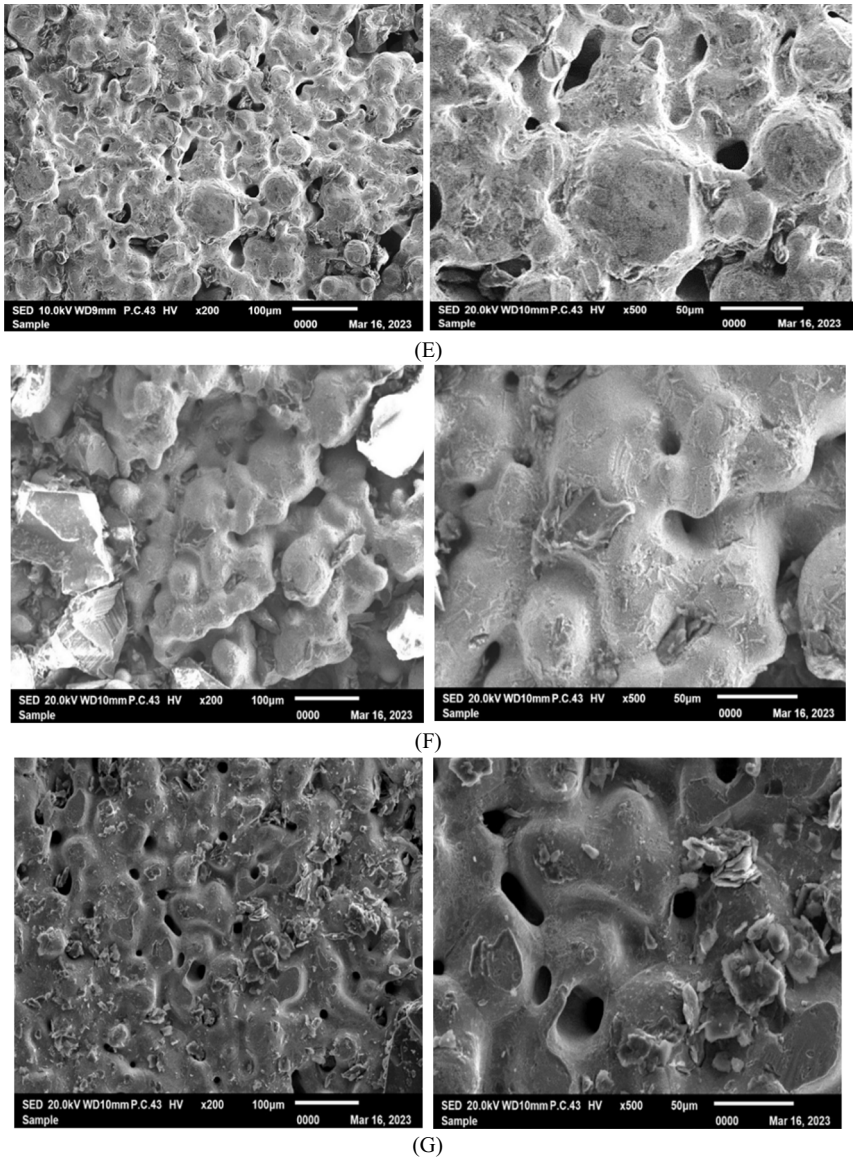


**Fig. 10** (continued)

After the sintering process of samples A, B, C, D, E, F, G, and H, sample C and sample G were properly sintered and retained their physical characteristics. while samples D and H did not fully sinter, resembling debinded materials. Sample D was extremely brittle, breaking easily and rendering it unsuitable for SEM analysis while Sample H became very soft, like clay, also preventing SEM analysis. The incomplete debinding of Samples D and H can be attributed to a single crucial factor, that is insufficient holding time. Initially, these samples were placed in Furnace 1, which was prematurely shut down due to technical issues. The limited holding time significantly affected the outcome of these samples. This concurrent experiment highlighted that the holding time emerged as the sole and most significant factor affecting the outcome of the samples.

After the sintering process of sample C, it was subjected to SEM analysis, and the microstructure showed that the metal grains were tightly packed and some were bonded, but still, the pores remained the same as shown in Fig. 10F. and sample G showed

**Table 14** Chemical Composition of Sintered Copper Samples

| Sample Name | Cu (%) | O (%) | Mg (%) | Ca (%) | S (%) |
|---|---|---|---|---|---|
| Sample A | 78.4 | 20.2 | 0 | 1.4 | 0 |
| Sample E | 55 | 28.6 | 7.7 | 5.6 | 3.1 |
| Sample B | 74.2 | 21.9 | 1.8 | 2.2 | 0 |
| Sample F | 79.9 | 17.6 | 0 | 2.5 | 0 |
| Sample C | 77.1 | 19.1 | 0 | 2.3 | 1.5 |
| Sample G | 50.1 | 30.1 | 5.3 | 9.8 | 4.7 |

significant copper particle diffusion but unfilled pores, indicating incomplete sintering (Fig. 10G). This is the result of incomplete sintering Samples A, E, B, and F that were debinded and sintered for a longer period of time in furnace 1 showed results similar to those of samples C and G in furnace 2, which were debinded and sintered for a shorter period of time but were still converted into a completed sintered sample like samples A, E, B, and F. Samples D and H were not able to be sintered in furnace 2 settings. It's critical to realize that utilizing shorter sintering and debinding durations may result in samples that are incomplete and of low quality. Holding the samples for a longer period will yield better results. The quality of the finished product could be compromised if the holding times are shortened.

#### *5.8.2 Energy dispersive X-ray (EDX) analysis for chemical composition*

The EDX analysis was conducted to determine the chemical composition of the sintered copper samples (A, E, B, F, C, and G) and compare them to the expected composition of the copper-polymer composite filament used for printing. Table 14 provides the chemical composition of sintered copper samples, detailing the weight percentages of copper (Cu), oxygen (O), magnesium (Mg), calcium (Ca), and sulfur (S). Samples A, B, F, and C exhibited high copper content, ranging from 74.2 wt% to 79.9 wt%, indicating successful printing and post-processing. However, the detection of oxygen suggests the potential presence of oxide layers formed during the sintering process. These oxides are attributed to exposure to ambient air during post-processing. EDX analysis revealed magnesium (Mg) contamination in Samples E (7.7%) and G (5.3%) (Table 14), likely introduced by the talc powder ($Mg_3Si_4O_{10}(OH)_2$) used during sintering, which contains ~ 19% Mg. Lower Mg levels in other samples (0–1.8%) suggest inhomogeneous talc contact or filament impurities. Calcium (Ca) and sulfur (S) traces may originate from the polymer binder or feedstock additives.

Significant oxygen contamination was found in the sintered samples by EDX analysis, which may have an adverse effect on their electrical conductivity. For example, Sample F had a slightly lower oxygen content of 17.6%, whereas Samples A and B had oxygen levels of 20.2% and 21.9%, respectively. The presence of oxygen is probably caused by oxide layers that formed in ambient air during the sintering process. Future research should consider performing debinding and sintering in controlled atmospheres, like nitrogen or argon, to reduce oxygen exposure and improve material purity in order to address this problem. By putting such circumstances into place, oxide production would be decreased, and the final goods' mechanical qualities and surface quality would be enhanced.

To mitigate the formation of oxides and enhance material purity, it is recommended to conduct the debinding and sintering processes in controlled atmospheres, such as

nitrogen, argon, or vacuum environments and use high-purity talc or inert ceramic supports to minimize cross-contamination. Such conditions would minimize oxygen exposure, reducing the formation of oxides and improving the mechanical properties and surface quality of the final product. Incorporating controlled atmospheres aligns with advancements in additive manufacturing and ensures higher consistency and reliability of sintered components. Future studies should focus on implementing controlled atmospheres during post-processing and evaluating their effects on the microstructure and mechanical properties of 3D-printed copper parts. This approach would further optimize the process and advance the field of metal extrusion additive manufacturing.

Although EDX analysis revealed high oxygen content (e.g., 20.2% in Sample A and 21.9% in Sample B), this did not consistently correlate with visible microstructural porosity. This suggests that the oxygen detected may be associated more with surface oxidation or light oxide layer formation rather than internal voids. However, carbon content was not quantified in this study due to the limitations of the EDX method used. Since carbon presence, whether as residue from binder degradation or atmospheric contamination, can influence both porosity and microstructural homogeneity, its absence from analysis is acknowledged as a limitation. Future studies are encouraged to employ CHNS analysis or XPS to examine carbon-related effects more accurately.

## 6 Conclusion and recommendation

In this study, we used a low-cost material extrusion 3D printer to effectively create copper-polymer composite parts, which we then debinded and sintered to achieve copper purity levels ranging from approximately 50% to nearly 80%. Our results demonstrate the importance of post-processing parameters, such as layer thickness, debinding time, and sintering duration, in influencing the printed parts' final quality. We discovered that the least amount of shrinkage (25.48%) was achieved while preserving high structural integrity when a 0.4 mm layer thickness was used in addition with a 4-h debinding and 5-h sintering process. This reduction is due to the stability of temperature gradients in thicker layers during debinding, which promotes uniform heat distribution, and the prolonged debinding period, which enables full binder removal, limiting residual stress-induced shrinking. However, thinner layers (0.3 mm) shrank more dramatically, demonstrating how crucial it is to adjust these parameters for optimal outcomes. Metal extrusion 3D printing can be a useful and affordable substitute for expensive technologies like powder bed fusion, according to one of the main findings of the research. By carefully optimizing post-processing conditions through the Taguchi method, we demonstrated that even affordable 3D printers can produce high-quality metal parts with the right approach. Our microstructural analysis confirmed good diffusion of copper particles, and the hardness tests showed that the samples had promising mechanical strength. There is still more potential for improvement in the future. Further research should concentrate on improving methods for removing binders, creating more precise yet reasonably priced 3D printers, and speeding up the debinding and sintering processes. Sintering in controlled environments may also enhance the overall performance and purity of the material. If these issues are resolved, material extrusion 3D printing has the potential to revolutionize sectors such as biomedical engineering, automotive, and aerospace, enabling more affordable, high-quality metal printing.

**Acknowledgements**
The authors acknowledge the support of International Islamic University Malaysia with equipment and facilities used in this research.

**Author Contribution**
Syed Fouzan Iftekar, Nor Aiman Sukindar, and Abdul Aabid wrote the main manuscript and Adibah Amir reviewed and edited the manuscript. Muneer Baig analysis and edited the manuscirpt.

**Funding**
This research is supported by the Structures and Materials (S&M) Research Lab of Prince Sultan University and the authors acknowledge the support of Prince Sultan University for paying the article processing charges (APC) of this publication.

**Data Availability**
Data is provided within the manuscript or supplementary information files.

## Declarations

**Ethics approval and consent to participate**
Not applicable.

**Consent to Publication**
Not applicable.

**Competing Interests**
The authors declare no competing interests.

Received: 2 January 2025 / Accepted: 8 September 2025
Published online: 15 October 2025

**References**

1. Shen X, Naguib HE. A robust ink deposition system for binder jetting and material jetting. Addit Manuf. 2019;29:100820. https://doi.org/10.1016/j.addma.2019.100820.
2. Iftekar SF, Aabid A, Amir A, Baig M. Advancements and limitations in 3D printing materials and technologies: a critical review. Polymers. 2023;15(11):2519. https://doi.org/10.3390/polym15112519.
3. Alzyod H, Takacs J, Ficzere P. Improving surface smoothness in FDM parts through ironing post-processing. J Reinf Plast Compos. 2023;43(11–12):671–81. https://doi.org/10.1177/07316844231173059.
4. Alzyod H, Ficzere P, Borbas L. Optimizing ironing parameters in material extrusion (MEX) technology: enhancing efficiency and performance. Discover Appl Sci. 2024. https://doi.org/10.1007/s42452-024-06249-7.
5. Alzyod H, Ficzere P. Neosanding postprocessing for improving surface roughness of extrusion-based 3D printing of PLA parts: a comparative analysis of stylus profilometer and confocal profilometry methods. J Braz Soc Mech Sci Eng. 2024;46(4):1–16. https://doi.org/10.1007/s40430-024-04817-x.
6. Alzyod H, Ficzere P. Ironing process optimization for enhanced properties in material extrusion technology using Box-behnken design. Sci Rep. 2024;14(1):1–14. https://doi.org/10.1038/s41598-024-52827-5.
7. Andreacola FR, Capasso I, Langella A, Brando G. 3D-printed metals: process parameters effects on mechanical properties of 17–4 P H stainless steel. Heliyon. 2023;9(7):e17698. https://doi.org/10.1016/j.heliyon.2023.e17698.
8. Raza, A., Waqar Ahmed, S., Hassan, A., Altaf, K., Wei, H., & Hussain, G. (2023). Investigation of the Process-Induced Defects in Metal Fused Deposition Modeling Process for Ultrafuse 316L Stainless Steel. Digital Manufacturing Technology, 250–261. https://doi.org/10.37256/dmt.3220233447
9. Nguyen TK, Lee B-K. Post-processing of FDM parts to improve surface and thermal properties. Rapid Prototyping J. 2018;24(7):1091–100. https://doi.org/10.1108/RPJ-12-2016-0207.
10. Drummond, M., Eltaggaz, A., Nouzil, I., & Deiab, I. (2023). Establishment of Select Printing Parameters for Low-Cost Fused Deposition Modeling Printed Cast Iron Through Experimental Optimization. 3D Printing and Additive Manufacturing. https://doi.org/10.1089/3dp.2023.0114
11. Lozhkomoev AS, Krinitcyn MG, Kazantsev SO, Vornakova EA, Svarovskaya NV, Glazkova EA. Development of approaches for forming complex profile parts from Al–Cu alloys using the metal fused filament fabrication technology. Prog Addit Manuf. 2024. https://doi.org/10.1007/s40964-023-00548-y.
12. Kolli S, Beretta M, Selema A, Sergeant P, Kestens LAI, Rombouts M, et al. Process optimization and characterization of dense pure copper parts produced by paste-based 3D micro-extrusion. Addit Manuf. 2023;73:103670. https://doi.org/10.1016/j.addma.2023.103670.
13. Khosravani MR, Ayatollahi MR, Reinicke T. Effects of post-processing techniques on the mechanical characterization of additively manufactured parts. J Manuf Process. 2023;107:98–114. https://doi.org/10.1016/j.jmapro.2023.10.018.
14. Atatreh S, Alyammahi MS, Vasilyan H, Alkindi T, Susantyoko RA. Evaluation of the infill design on the tensile properties of metal parts produced by fused filament fabrication. Results Eng. 2023;17:100954. https://doi.org/10.1016/j.rineng.2023.100954.
15. Shamsudin S, Ali A, Kamarudin K, Al-Alimi S, Altharan YM, Ibrahim M. Biocompatibility and strength tests of PLA/SS316L composite material for orthopedic implant applications utilizing the 3D printing technique. AIP Conf Proc. 2023. https://doi.org/10.1063/5.0183829.
16. Wu S, Li H, Han C, Wu W. Effects of full chain processes on the performance of 316L stainless steel composite by fused deposition modeling and sintering. Metals. 2023;13(12):2022. https://doi.org/10.3390/met13122022.

17. Silvain J-F, Gifford DL, Fourcade S, Cuzacq L, Grosseau-Poussard J-L, Debiemme-Chouvy C, et al. Study on debinding and sintering conditions in extrusion-based additive manufacturing of 316L and 316L + Cu. Metals. 2023;13(11):1858. https://doi.org/10.3390/met13111858.
18. Mogan J, Sandanamsamy L, Harun WSW, Ishak I, Romlay FRM, Kadirgama K, et al. Thermo-mechanical properties of ABS/stainless steel composite using FDM. Mater Today Proc. 2024. https://doi.org/10.1016/j.matpr.2024.01.029.
19. Opoz TT, Burgess A, Ahuir-Torres JI, Kotadia HR, Tammas-Williams S. The effect of surface finish and post-processing on mechanical properties of 17–4 PH stainless steel produced by the atomic diffusion additive manufacturing process (ADAM). Int J Adv Manuf Technol. 2024;130(7–8):4053–66. https://doi.org/10.1007/s00170-024-12949-6.
20. Sadaf M, Bragaglia M, Slemenik Perše L, Nanni F. Advancements in metal additive manufacturing: a comprehensive review of material extrusion with highly filled polymers. J Manuf Mater Process. 2024;8(1):14. https://doi.org/10.3390/jmmp8010014.
21. Rajendran S, Palani G, Kanakaraj A, Shanmugam V, Veerasimman A, Gądek S, et al. Metal and polymer based composites manufactured using additive manufacturing—a brief review. Polymers (Basel). 2023;15(11):2564. https://doi.org/10.3390/polym15112564.
22. Kumar N, Soren S, Prasad R, Singh Y, Nautiyal H, Sharma A, et al. Optimization of sintering process parameters by Taguchi method for developing Al-CNT-reinforced powder composites. Crystals. 2023;13(9):1352. https://doi.org/10.3390/cryst13091352.
23. Gonzalez-Gutierrez J, Cano S, Ecker JV, Kitzmantel M, Arbeiter F, Kukla C, et al. Bending properties of lightweight copper specimens with different infill patterns produced by material extrusion additive manufacturing, solvent debinding and sintering. Appl Sci. 2021;11(16):7262. https://doi.org/10.3390/app11167262.
24. Agrawal AP, Kumar V, Kumar J, Paramasivam P, Dhanasekaran S, Prasad L. An investigation of combined effect of infill pattern, density, and layer thickness on mechanical properties of 3D printed ABS by fused filament fabrication. Heliyon. 2023;9(6):e16531. https://doi.org/10.1016/j.heliyon.2023.e16531.
25. Suwanpreecha C, Manonukul A. A review on material extrusion additive manufacturing of metal and how it compares with metal injection moulding. Metals. 2022;12(3):429. https://doi.org/10.3390/met12030429.
26. Artillery - X. (2019). Artillery Sidewinder-X1 3D Printer. https://www.aliexpress.com/i/1005001471234376.html
27. Cherdo, L. (2024, April 6). Markforge Metal X 3D printer. https://www.aniwaa.com/product/3d-printers/markforged-metal-x/#:~:text=Description,provided%20information%20and%20public%20data.
28. MSE Supplies. (2024). Nabertherm 1400°C High Performance High Temperature Muffle Furnace L(T) 5/14. https://www.msesupplies.com/products/high-performance-nabertherm-1400-c-high-temperature-muffle-furnace-lt-5-14?variant=39563924013114
29. Chang G, Zhang X, Ma F, Zhang C, Xu L. Printing, debinding and sintering of 15–5PH stainless steel components by fused deposition modeling additive manufacturing. Materials. 2023;16(19):6372. https://doi.org/10.3390/ma16196372.
30. Scendo M, Zorawski W, Staszewska-Samson K, Goral A. Influence of laser treatment on the corrosion resistance of Cr3C2-25(Ni20Cr) cermet coating. Materials. 2021;14(15):4078. https://doi.org/10.3390/ma14154078.
31. Chen S, Xiao C, Liu K, Li N, Khan SB, Wu J, et al. Investigation of debinding sintering strategy and analysis of different structure properties of printed ceramic clay materials based on liquid deposition molding technology. Discover Appl Sci. 2024;6(3):106. https://doi.org/10.1007/s42452-024-05753-0.
32. Ali A, Zhang N, Santos RM. Mineral characterization using scanning electron microscopy (SEM): a review of the fundamentals, advancements, and research directions. Appl Sci. 2023;13(23):12600. https://doi.org/10.3390/app132312600.
33. Sakib-Uz-Zaman C, Khondoker MAH. A review on extrusion additive manufacturing of pure copper. Metals. 2023;13(5):859. https://doi.org/10.3390/met13050859.


## Publisher's Note